RESEARCH ARTICLE

Key Points:
- Natural variability drives strong fluctuations in dissolved oxygen within the ocean interior
- Natural variability challenges detection of forced trends in dissolved oxygen
- Time of emergence of forced trends is quantified based on state, trends, and spatial patterns

Correspondence to:
M. C. Long,
mclong@ucar.edu

Finding forced trends in oceanic oxygen

Matthew C. Long[1], Curtis Deutsch[2], and Taka Ito[3]

[1]National Center for Atmospheric Research, Boulder, Colorado, USA, [2]School of Oceanography, University of Washington, Seattle, Washington, USA, [3]Earth and Atmospheric Sciences, Georgia Institute of Technology, Atlanta, Georgia, USA

Abstract Anthropogenically forced trends in oceanic dissolved oxygen are evaluated in Earth system models in the context of natural variability. A large ensemble of a single Earth system model is used to clearly identify the forced component of change in interior oxygen distributions and to evaluate the magnitude of this signal relative to noise generated by internal climate variability. The time of emergence of forced trends is quantified on the basis of anomalies in oxygen concentrations and trends. We find that the forced signal should already be evident in the southern Indian Ocean and parts of the eastern tropical Pacific and Atlantic basins; widespread detection of forced deoxygenation is possible by 2030–2040. In addition to considering spatially discrete metrics of detection, we evaluate the similarity of the spatial structures associated with natural variability and the forced trend. Outside of the subtropics, these patterns are not wholly distinct on the isopycnal surfaces considered, and therefore, this approach does not provide significantly advanced detection. Our results clearly demonstrate the strong impact of natural climate variability on interior oxygen distributions, providing an important context for interpreting observations.

1. Introduction

Dissolved oxygen is a critical constituent in the marine environment, strongly regulating metabolic and biogeochemical processes. Anthropogenic climate change is projected to drive deoxygenation over much of the ocean [*Bopp et al.*, 2002; *Keeling and Garcia*, 2002; *Plattner et al.*, 2002; *Cocco et al.*, 2013] with potentially serious side effects, including deleterious impacts on marine biota and disruptions to the biogeochemical cycles of key elements [*Keeling et al.*, 2010; *Doney et al.*, 2014]. Oxygen in the ocean interior is consumed by respiration of sinking organic matter and replenished via the advection and mixing of oxygen-enriched surface waters [*Keeling and Garcia*, 2002]. Ocean warming reduces O_2 solubility, depleting surface concentrations; furthermore, warming-induced stratification curtails surface-to-depth exchange, diminishing supply of O_2 to the interior.

Numerous attempts have been made to detect low-frequency variability and long-term trends in O_2 observations from ocean time series [e.g., *Ono et al.*, 2001; *Andreev and Baturina*, 2006; *Whitney et al.*, 2007], repeat hydrographic sections [e.g., *Emerson et al.*, 2004; *Johnson and Gruber*, 2007; *van Aken et al.*, 2011; *Sasano et al.*, 2015], or compilation and optimal interpolation of historic observations [e.g., *Stramma et al.*, 2008; *Helm et al.*, 2011; *Stendardo and Gruber*, 2012]. The historical database presents significant challenges for these analyses, including both sparse and irregular sampling over space and time, as well as potential changes in methods and calibration over time. For example, *Stanley et al.* [2012] document an apparent oxygen decline from the 1980s to 2000s in the North Atlantic subtropical mode water at the Bermuda Atlantic Time Series (BATS) site. The authors found a decrease in $[O_2]$ and increase in apparent oxygen utilization within upper ocean isopycnals; but they also show that the ventilation metric (mean age constrained by tritium-helium observations) did not change significantly and — based on scatter in the historical oxygen data not reflected in temperature and salinity — conclude that the $[O_2]$ change may be an artifact of measurement errors.

While statistically significant trends in interior $[O_2]$ distributions have been observed in specific oceanic regions, and in some cases over long time periods (50 years) [*Bograd et al.*, 2008; *Stendardo and Gruber*, 2012], attribution of these trends to externally forced climate change is also challenged by the presence of significant background "noise" associated with internally driven, low-frequency climate variability [*Garcia et al.*, 2005; *Ito and Deutsch*, 2010]. Internal variability is a natural, intrinsic feature of the coupled atmosphere-ocean-land system, arising from nonlinear dynamical processes, and interactions between climate system components that integrate forcing over different timescales [*Hasselmann*, 1976]. The broadband fluctuations of the climate

system impart variability to oceanic O_2 distributions by inducing thermally driven surface anomalies, modulating surface-to-depth exchange, and altering the structure of the upper ocean environment, thereby impacting organic matter production and subsequent oxygen utilization rates (OUR) in the interior [*Ito and Deutsch*, 2010; *Deutsch et al.*, 2011]. A recent study using historic data and repeat sections in the Labrador Sea, for instance, linked the regional [O_2] variability to deep ventilation events driven by variation in convective mixing occurring on decadal or shorter timescales [*van Aken et al.*, 2011]. Oxygen in the subpolar North Pacific also displays significant variability [*Deutsch et al.*, 2006], which has been linked to fluctuations in the winter time atmospheric forcing of the ocean [*Andreev and Baturina*, 2006].

The variability in oxygen driven by internal climate fluctuations amounts to noise; changes driven by increasing greenhouse gas concentrations are superimposed on natural variability, making detection of forced trends a signal-to-noise problem. For detection to be possible, forced signals must develop magnitude and persistence sufficient to transcend the noise, the envelop of background variability [*Hasselmann*, 1993; *Santer et al.*, 1994, 2011]. In this context, internally generated variability inherently limits detection of climate-change signals regardless of practical observing capabilities; inferring trends from sparse observations is an obvious additional complication.

In this paper, we use an Earth system modeling framework to quantify detectability—or the "Time of Emergence" (ToE)—of the anthropogenic climate change signal in oceanic [O_2]. Earth system models consist of coupled atmosphere-ocean general circulation models (GCMs) and represent processes relevant to the global carbon cycle, including the lower trophic levels of marine ecosystems. The coupled GCMs spontaneously generate internal variability representative of the real climate system and are forced with historical and future scenario data sets defining anthropogenic effects, thus providing a powerful means of examining mechanisms by which climate variability and change impact ocean biogeochemistry. Our objectives are to quantify and understand the controls on the ToE for oceanic [O_2] signals, with the hope of gaining insight into where and when early climate change signals might be detectable. Observational programs guided by such insight might target nascent signals to reduce uncertainty in the nature, magnitude, and impact of climate change on marine ecosystems, thereby providing a more reliable basis for adaptation strategies and understanding cost/benefit trade-offs associated with climate change mitigation.

We employ a relatively novel Earth system modeling approach to address these objectives. Rather than analyzing an ensemble of opportunity comprised of model integrations from several independently developed models, we make use of a "large" ensemble of integrations conducted with a single Earth system model (the Community Earth System Model; CESM). In the typical multi-model ensemble, spread reflects structural differences among the models, as well as intrinsic climate variability. The advantage of an ensemble from a single model is that spread arises purely from internally-generated variability. If the ensemble is sufficiently large, the ensemble mean provides a robust estimate of the deterministic, forced signal and the ensemble spread is indicative of the noise, inclusive of changes in variance that may occur as function of climate state [*Deser et al.*, 2012]. In addition to results from CESM, we include an examination of oxygen ToE in the recent Coupled Model Intercomparison Project, phase 5 (CMIP5) [*Taylor et al.*, 2012], thereby placing the CESM results in the broader context of recent Earth system models.

This paper is organized as follows. In the next section, we describe the model configurations and experimental setup. In section 3 we define and present the metrics of ToE applied to the Earth system model results. Finally, we summarize these results and conclude in section 4.

2. Models and Numerical Experiments

2.1. Model Description

We analyze fields from the CESM Large Ensemble (CESM-LE) experiment [*Kay et al.*, 2014]. The CESM-LE included 30 simulations, 24 of which (numbers 1, 2, and 9–30) include ocean biogeochemistry output. *Kay et al.* [2014] provide a detailed description of the coupled model configuration. Briefly, the atmosphere component was the Community Atmospheric Model, version 5 (CAM5), integrated at nominal 1°×1° horizontal resolution [*Hurrell et al.*, 2013]. The ocean component is based on the Parallel Ocean Program, version 2 [*Smith et al.*, 2010], integrated with a nominal horizontal resolution of 1°×1° and 60 vertical levels [*Danabasoglu et al.*, 2012]. The sea ice component is the Los Alamos Sea Ice Model, version 4 [*Hunke and Lipscomb*, 2008] with some updates including prognostic melt ponds and the deposition and cycling of black carbon and dust aerosols [*Holland et al.*, 2012]. The ocean biogeochemistry module is known as the
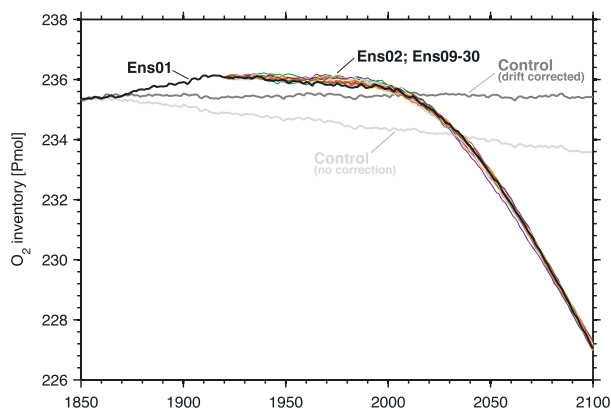
Figure 1. Time series of annual mean global dissolved O_2 inventory in the CESM Large Ensemble experiment. The light gray line shows the 1850 control without drift correction; the dark gray line is the 1850 control after removal of the linear trend associated with model drift. The black line is ensemble member 1, and the colored lines show the remaining ensemble members; all time series associated with the transient integrations have been corrected for linear drift in the 1850 control.

Biogeochemical Elemental Cycling (BEC) model, which includes three phytoplankton functional types (diatoms, "small" picophytoplankton/nanophytoplankton, and diazotrophs) and one adaptive zooplankton class [*Moore et al.*, 2013]. Phytoplankton growth is determined as a function of temperature, multinutrient (N, P, Si, and Fe) limitation, and light availability. Remineralization is computed following the *Armstrong et al.* [2002] ballast association model. In the CESM-LE, BEC was configured to have no impact on the physical state of the model (shortwave absorption was computed using a fixed chlorophyll climatology) [*Long et al.*, 2015]. *Long et al.* [2013] and *Moore et al.* [2013] review the performance of the BEC model version in CESM integrations contributed to CMIP5 and find that simulations compare favorably to observations for many carbon cycle and surface productivity metrics. We discuss the model's simulation of dissolved oxygen in detail below.

2.2. Numerical Experiments

The CESM-LE experiment began with an 1850 control integration in which external forcings (i.e., CO_2 mixing ratio, aerosols, etc.) were held constant at preindustrial levels. The ocean in the 1850 control was initialized from a state of rest with modern observationally based temperature and salinity fields, while ocean biogeochemical tracers were taken from an independent 600 year spin up integration; other component models were initialized from a previous CESM (CAM5) simulation. Ensemble member 1 (Ens01) was initialized from the 1850 control at a randomly chosen year (402), after the model was deemed to be sufficiently close to quasi-equilibrium. Ens01 was integrated from 1850 through 2100 forced by historical data sets through 2005 and then the CMIP5 Representative Concentration Pathway 8.5 (RCP8.5) for 2006–2100 [*Meinshausen et al.*, 2011]. The model CO_2 forcing was concentration based: the atmospheric CO_2 mixing ratio was specified, not solved for prognostically with emissions specified. Additional ensemble members (Ens02–Ens30) were initialized from Ens01 at 1 January 1920 and integrated with identical external forcing. Ensemble member 2 (Ens02) began with an ocean initial state lagged by 1 day; the remaining ensemble members (Ens03–Ens30) were initialized with round-off level ($\mathcal{O}(10^{-14})$ K) perturbations applied to the air temperature field. This methodology introduces sufficient variation such that dominant modes of climate variability are out of phase within a decade or so. The CESM-LE does not sample variation in ocean initial conditions; this is justified under the hypothesis that memory of ocean initial conditions does not last beyond about a decade [*Branstator and Teng*, 2010], thus perturbation of atmospheric air temperature samples most of the internal variability [*Deser et al.*, 2012].

Figure 1 shows the time evolution of the global oceanic O_2 inventory in the CESM-LE (Ens03–Ens08 did not have ocean biogeochemistry output). During the period of the control simulation corresponding to 1850–2100, the global oceanic O_2 inventory was still drifting at a rate of -0.0074 Pmol yr^{-1}; this drift has been removed from all series corresponding to transient integrations in Figure 1. Between 1850 and 1920, the global oxygen inventory in Ens01 increased slightly (~0.3%) due to a global cooling signal that is clearly outside the range of interannual variability evident in the control simulation. The cooling is attributable to transient aerosol and volcanic forcing present in the historical simulation but not in the control.
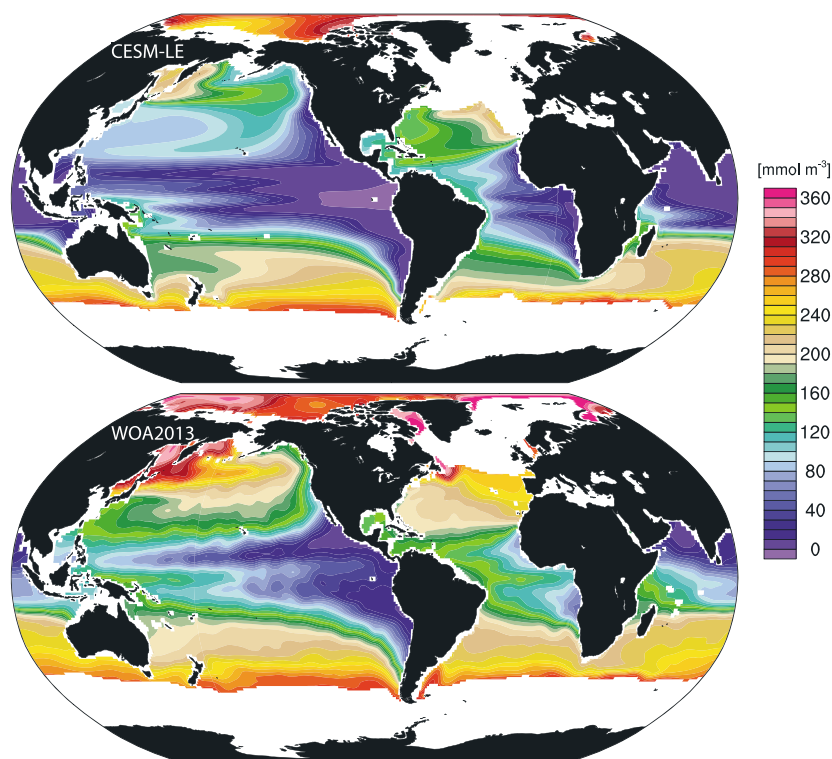
Figure 2. Annual mean dissolved oxygen concentration on the $\sigma_\theta = 26.5$ potential density surface. (top) The ensemble mean from the CESM-LE over the period 1981–2000; (bottom) The optimally interpolated annual mean climatology from the World Ocean Atlas, 2013 [*Garcia et al.*, 2014].

2.3. Model Validation

We haven chosen to analyze properties on isopycnal surfaces, thereby excluding substantial interannual variability in tracers relative to a depth framework, which is subject to variability derived from isopycnal heave. For simplicity, we focus the analysis on the $\sigma_\theta = 26.5$ potential density surface, which is at a average depth of ~ 290 m in the CESM-LE at 1920 and is largely representative of the core of the main ventilated thermocline in the present climate. An isopycnal framework naturally emphasizes ventilation and biological consumption effects on [O_2] distributions over solubility effects, since temperature plays a major role in setting the density of seawater, and thus, changes in solubility are muted on surfaces of constant density.

Figure 2 shows annual mean dissolved oxygen on the $\sigma_\theta = 26.5$ potential density surface from the CESM-LE and the World Ocean Atlas (WOA) [*Garcia et al.*, 2014], an observationally based, gridded climatology. The observed large-scale spatial pattern of [O_2] is well represented by CESM (pattern correlation, $r = 0.93$), though it tends to be biased low (mean bias = -44; RMS error = 56 mmol m^{-3}). Negatively biased model [O_2] is widespread in the tropics, where the model oxygen minimum zones (OMZs) are too extensive [*Moore et al.*, 2013]. This bias is common in coarse-resolution ocean GCMs and is partially attributable to sluggish circulation yielding weak ventilation [*Brandt et al.*, 2008, 2012; *Dietze and Loeptien*, 2013; *Getzlaff and Dietze*, 2013; *Duteil et al.*, 2014]. The extent of OMZs is also sensitive to the prescribed remineralization profile for sinking organic matter, as well as the stoichiometric ratios used for growth and remineralization of organic matter [*Devries and Deutsch*, 2014]. While ventilation in the midlatitude Southern Ocean appears to be reasonable, the model's western North Pacific is strongly deficient in O_2. This may be due in part to a poor representation of diapycnal mixing over rough topography [*Nakamura et al.*, 2006].

The importance of ventilation in controlling the mean oxygen distribution is evident in the relationship between water mass age and [O_2]. Outside of the tropics, the mean [O_2] is tightly related to "ideal age" (pattern correlation, $r = -0.86$; Figure 3). Ideal age is a tracer that provides a metric of time since last contact with the surface; it is set to zero at the surface and increases at 1 yr yr^{-1} in the interior. Freshly ventilated waters
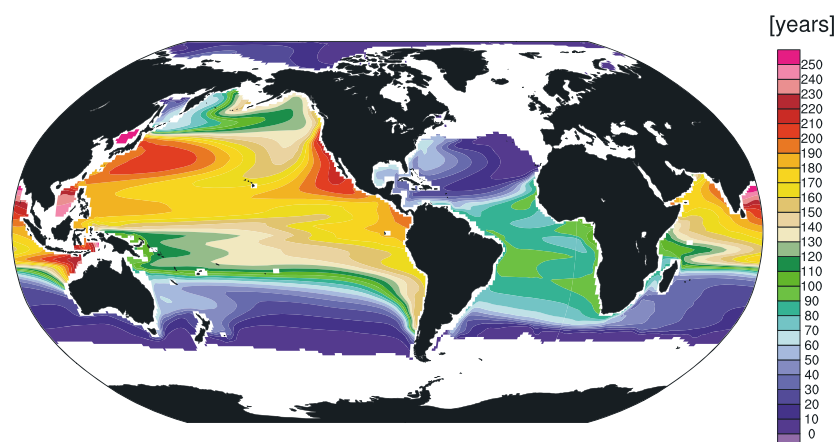
Figure 3. Ideal age distribution on the σ_θ=26.5 potential density surface from the CESM-LE ensemble mean over the period 1981–2000.

are relatively rich in O_2; as water masses age in the ocean interior, a respiration signal accumulates, leading to an inverse correlation between [O_2] and age. This relationship breaks down in the tropics, where O_2 depletion overwhelms the oxygen supply and concentrations are drawn down to near zero (Figure 2).

There are many factors that limit the ability of the model to accurately capture observed variability. The relatively coarse resolution ($\mathcal{O}(100)$ km) precludes representation of smaller-scale processes such as oceanic mesoscale eddies, which drive relatively high frequency fluctuations of biogeochemical properties. Biases in the mean state are likely to also impact simulated variability. For example, if spatial gradients in [O_2] are too weak in the mean state, then anomalous circulation or mixing will yield temporal [O_2] anomalies that are also too weak. There are relatively few locations where the variance of [O_2] can be accurately estimated from observations. However, a comparison of the magnitude of interannual variability from the Hawaii Ocean Time-Series (HOT) station and the same location in CESM demonstrates that CESM does indeed have weaker variability. The standard deviation of the annually binned and detrended dissolved O_2 concentrations on the $\sigma_\theta = 26.5$ surface in the observations is about 5.5 mmol m^{-3}, whereas CESM has a standard deviation of about 2.4 mmol m^{-3} (Table 1).

Table 1. Observed and Modeled Oxygen Trends at Three Ocean Time Series Stations: Hawaii Ocean Time (HOT) Series in the Subtropical Pacific, Ocean Station Papa (OSP) in the Eastern Subpolar North Pacific, and the Bermuda Ocean Time Series (BATS) in the Western Subtropical Atlantic[a]

Station	HOT (1988–2014)		OSP (1956–2006)		BATS (1988–2012)	
σ_θ	25.2	26.5	26.5	26.7	26.5	26.8
N (obs)	624	621	370	339	364	344
Median (obs)	194.2	141.2	216.1	177.4	198.3	174.2
SD (obs, raw)	16.2	23.3	25.9	23.6	7.31	13
SD (obs, ann)	4.38	5.46	17.5	16.1	4.94	6.49
Trend (obs)	-0.32 ± 0.12	-1.19 ± 0.12	-0.57 ± 0.19	-0.64 ± 0.14	0.03 ± 0.14	-0.42 ± 0.17
Median (CESM)	195	109	136	70.8	139	122
SD (CESM, ann)	1.92	2.38	10.2	4.41	5.16	0.721
Trend (CESM)	-0.05 ± 0.09	-0.02 ± 0.22	0.05 ± 0.22	-0.00 ± 0.12	-0.11 ± 0.23	0.00 ± 0.07
Trend range (CESM)	$-0.23, 0.09$	$-0.37, 0.28$	$-0.29, 0.42$	$-0.16, 0.16$	$-0.43, 0.26$	$-0.10, 0.10$

[a]Standard deviations are computed on all observations (raw) and detrended annual mean data (ann). Linear trends are computed on annual mean data. Standard error of the trend on the observations is estimated by bootstrapping methods in which the annual mean data is randomly sampled to form 50 subsamples. The trend error in the model is the standard deviation of trends across the ensemble. The trend range shows the 5th and 95th percentile trends computed from the CESM-LE. Units are mmol m^{-3} for concentration and mmol m^{-3} yr^{-1} for trends.

2.4. CMIP5 Models

We selected a small group of CMIP5 models to provide context for the CESM-LE results. The models are GFDL-ESM2M from the Geophysical Fluid Dynamics Laboratory (GFDL) [*Dunne et al.*, 2012, 2013]; HadGEM2 from the UK Met Office Hadley Centre [*Collins et al.*, 2011; *HadGEM2 Development Team*, 2011]; and MPI-ESM from the Max Planck Institute (MPI) [*Giorgetta et al.*, 2013]. We used 1850 control simulations to evaluate variability of $[O_2]$ under an unperturbed climate state. Historical simulations were used from 1850–2005, followed by RCP8.5 simulations through 2100. A single integration from the GFDL model was used, whereas small ensembles were available from HadGEM2 ($n=5$) and MPI ($n=3$).

3. Analysis

As discussed in section 1 above, the ability to distinguish a forced signal from natural variability is central to the problem of detection. There are three elements of the time-evolving signal-to-noise relationship that can be considered [*Santer et al.*, 1994]. First, the change in the mean value of the state variable of interest may be compared to the temporal variance in the unforced (or control) climate; external forcing can be identified if the state of the system falls outside the range of unforced variability [*Christian*, 2014]. Second, the magnitude of trends in a temporally varying signal can be compared to the variance in trends in the control climate; detection occurs when the trend magnitude falls sufficiently far outside the natural distribution of trends. Finally, the similarity of the spatial structure associated with forced signals can be evaluated relative to the dominant spatial structures associated with natural variability; detection in this context relies on the extent to which the pattern associated with a forced signal is distinct from the patterns associated with natural variability.

Following *Hasselmann* [1993], a time-evolving spatial pattern of a climate variable in a particular forced transient simulation *i* can be represented as

$$\psi_i(x,t) = \psi^s(x,t) + \tilde{\psi}_i(x,t),$$

where $t = 1, \ldots, n$ and $x = 1, \ldots, p$ denote discrete time (annual means) and space (model grid points). $\psi^s(x,t)$ is the forced, deterministic climate signal, whereas $\tilde{\psi}_i(x,t)$ is the component due to intrinsic variability and hence unique to each ensemble member in the set $i = 1, \ldots, m$. Similarly, in the 1850 control integration that has no transient forcing, we have

$$c(x,t) = \tilde{c}(x,t),$$

where the time evolution is purely due to intrinsic variability, presuming that the model is in stationary equilibrium. In practice, it is necessary to account for model drift; in all subsequent analyses, we do this by subtracting a linear trend computed from the control simulation. Model drift indicates that interior ocean tracer fields are not at equilibrium with respect to the circulation; while it would be desirable to integrate the model for longer prior to spawning transient runs, this was not feasible within the time constraints of the CESM-LE experiment. However, while the drift is undesirable, it does not preclude analysis of the transient integrations. Inspection of the CESM-LE control shows that the drift is well approximated by a linear fit for all variables of interest over the period in the control integration corresponding to 1920–2100 (model years 472–652). Unfortunately, while the CESM-LE control was integrated for an additional ~1500 years beyond the period corresponding to 1920–2100 (for total of 2200 years), drift in interior oxygen and other variables is not linear over the whole run; it is therefore difficult to treat variables in the control as homogenous time series. For this reason, we restrict our analysis of the control integration to the period corresponding to 1920–2100 where we are confident that drift is linear and its removal is robust.

In the CESM-LE, we can estimate $\psi^s(x,t)$ as the average across the ensemble,

$$\psi^s(x,t) = \frac{1}{m}\sum_{i=1}^{m}\psi_i(x,t), \tag{1}$$

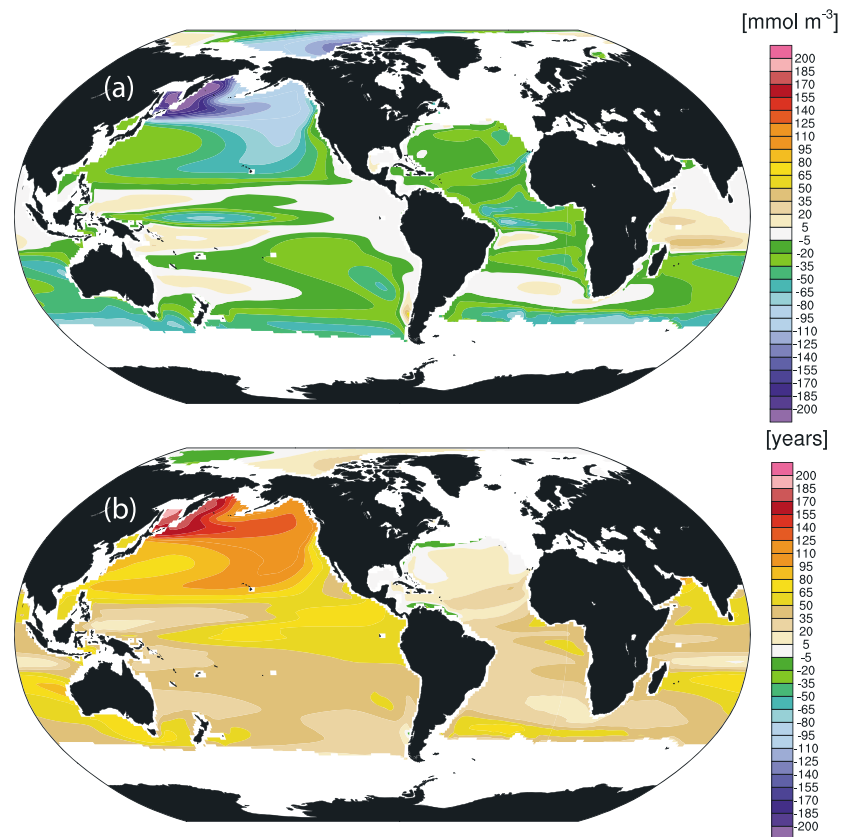since *m* is sufficiently large [*Deser et al.*, 2012].

Figure 4. Change between the periods 1981–2000 and 2081–2100 in (a) dissolved oxygen and (b) ideal age on the σ_θ = 26.5 potential density surface in the CESM-LE ensemble mean.

We present results from annually averaged data, interpolated from the model grid to a 1°×1° regular latitude, longitude grid—or to a point for comparison to data at ocean times series locations. In some cases, we use time-evolving climate anomalies, defined as

$$\psi_i'(x, t) = \psi_i(x, t) - \bar{c}(x)$$

and

$$c'(x, t) = c(x, t) - \bar{c}(x),$$

where $\bar{c}(x)$ is the long-term mean of the (drift-corrected) control.

The choice of an isopycnal versus depth framework has implications for interpreting signals associated with climate warming. In particular, warming manifests as movement of isopycnal surfaces deeper into the ocean interior; thus, the isopycnal framework highlights deoxygenation mechanisms other than solubility-driven changes in [O_2] that might dominate at a given near-surface depth horizon. The $\sigma_\theta = 26.5$ surface deepens by about 120 m in the Subarctic North Pacific by the end of RCP8.5 in the CESM-LE; it deepens by more than 300 m in regions of the Southern Ocean equatorward of the present-day outcrop. The detection of the solubility signal can be directly evaluated from temperature trends. Our approach thus focuses on the detection of the most uncertain part of the deoxygenation signal, that associated with changes in circulation and respiration.

3.1. Overview of Transient Simulations

In this section we describe some broad features of the simulated change and variability in [O_2], providing context for understanding detectability. Figure 4 shows the change in [O_2] between the late twentieth century and the end of the 21st century in the CESM-LE. Oxygen depletion on the $\sigma_\theta = 26.5$ surface is most pronounced in the western North Pacific, which is a prominent ventilation site for this isopycnal (Figure 3). Reductions in [O_2] over much of the North Pacific and extratropics generally are strongly associated with increases in ideal age (Figure 4b), indicating that enhanced stratification and diminished O_2 supply are dominant mechanisms contributing to interior deoxygenation. Indeed, extratropical change in age and [O_2] are
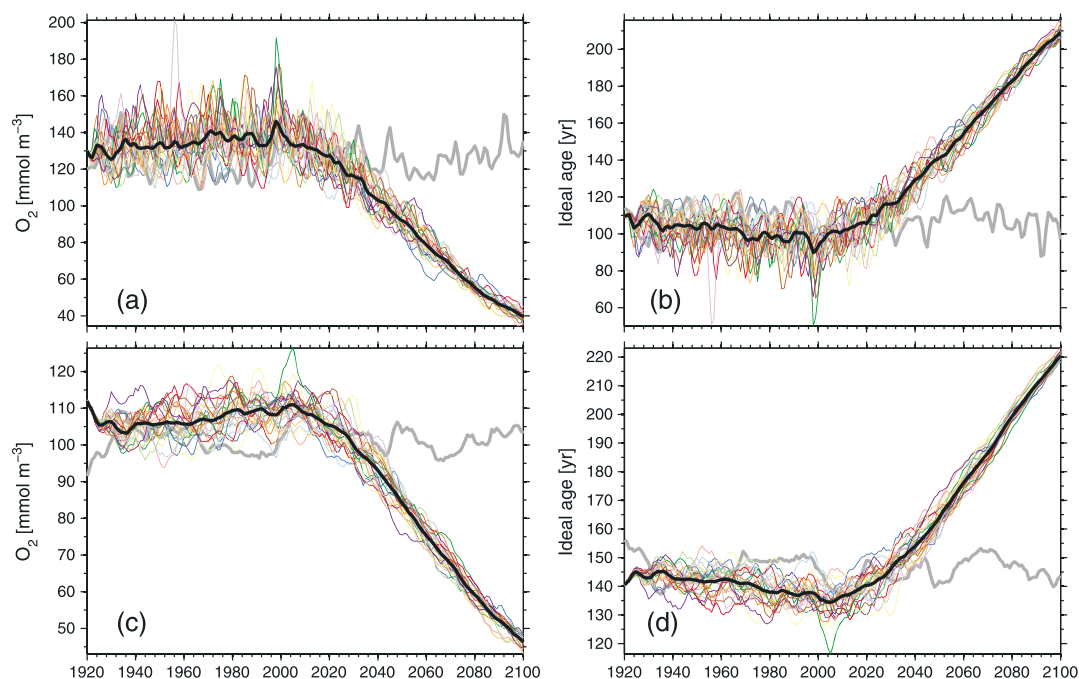
Figure 5. Time series of O_2 and ideal age on the $\sigma_\theta = 26.5$ potential density surface in the CESM-LE integrations at locations corresponding to (a, b) Ocean Station Papa (50°N, 145°W) and (c, d) the Hawaii Ocean Time-Series Station Aloha (22.75°N, 158°W). The gray line shows the control simulation, while the black line is the ensemble mean; the other lines show individual ensemble members.

significantly correlated (pattern correlation, $r = -0.76$). While there is a substantial increase in ventilation age in the eastern equatorial Pacific (Figure 4b), this is not associated with strong declines in $[O_2]$ since this region is characterized by near-zero $[O_2]$ in the present-day climate simulations (Figure 2). Certain regions on the $\sigma_\theta = 26.5$ surface show near-zero change or even weak increases in $[O_2]$, including much of the western Pacific and south Atlantic basins as well as virtually all of the tropical Indian Ocean (Figure 4a). These regions are not associated with reductions in age but are responding to a weak (salinity compensated) cooling of the $\sigma_\theta = 26.5$ surface, with magnitudes as much as $-2°C$ north of New Zealand in the south Pacific (not shown). In addition to cooling, reductions in OUR contribute to localized $[O_2]$ increases. OUR declines virtually everywhere in the CESM-LE on $\sigma_\theta = 26.5$, primarily driven by reductions in surface primary productivity [*Moore et al.*, 2013]. Furthermore, organic matter fluxes and remineralization rates decay exponentially with depth; thus, OUR is reduced on a given isopycnal surface as that surface moves downward with ocean warming.

The temporal evolution of $[O_2]$ at locations corresponding to the Hawaii Ocean Time-Series Station Aloha (HOT) and Ocean Station Papa (OSP) illustrates the type of variability and trends present on local scales in the CESM-LE simulation (Figure 5). A period of time following 1920 is required for the ensemble spread to fully develop, most notable at HOT where it takes 10–15 years (Figure 5c). Following this initial inflation period, the spread remains relatively constant and only weak trends are present in the ensemble mean until about the year 2010; after this point, O_2 concentrations begin to decline precipitously. The decline in $[O_2]$ is closely associated with an increase in ideal age at HOT and OSP (Figure 5bd), consistent with a diminished supply of freshly ventilated waters being the dominant mechanism driving deoxygenation. In addition to the long-term climate change signal, interannual variability in $[O_2]$ at HOT and OSP on the 26.5 isopycnal surface is also closely related to variability in ventilation age; indeed, variation in ideal age explains 86% of the variance in $[O_2]$ at HOT and 93% at OSP in CESM-LE integrations over the period 1920–2000, which is prior to the onset of substantial deoxygenation. Interannual variability in $[O_2]$ is also significantly related to density-compensated changes in temperature and salinity ("spice"), though these relationships are much weaker than for age. Variation in spice may reflect anomalies in surface forcing and ventilation but can additionally indicate variability introduced by lateral mixing along isopycnal surfaces in the ocean interior. The overall variability in $[O_2]$ is greater at OSP (Table 1); temperature, salinity, ideal age and OUR also show greater variability at OSP. Increased variability at OSP partially reflects the younger ventilation age (Figure 5) and the shallower depth

of the 26.5 isopycnal surface at this location (~200 m) relative to its depth at HOT (520 m). A shallower depth yields greater susceptibility to direct perturbation by anomalous surface forcing.

Metrics of [O_2] variability and trends within thermocline and intermediate waters from major ocean time series stations are listed in Table 1. In all stations, variability on subannual timescales is strongly influenced by transient phenomena, such as mesoscale eddies; data averaged to annual timescales show diminished variability. Observations from all stations and isopycnal surfaces shown display statistically significant negative trends in [O_2], with the exception of the "18°" water in the North Atlantic ($\sigma_\theta = 26.5$ at BATS). Central Mode Water in the North Pacific ($\sigma_\theta = 26.5$ at HOT) exhibits the strongest negative trends (-1.19 ± 0.12 mmol O_2 m^{-3} yr^{-1}). As discussed above, the CESM-LE has interannual variability that is weaker than observed at most locations on Table 1; furthermore, all the observed trends that are statistically significant have magnitudes that fall outside the range of trends (5th–95th percentile) at the same location in the CESM-LE. This may suggest that the model is not sufficiently sensitive to climate forcing, either in the form of internally generated or forced variability (see section 4).

An interesting feature accompanying the 21st century decline in [O_2] in the CESM-LE is the reduction in ensemble spread (Figure 5). A reduction in ensemble spread might be expected from increased ventilation age, which is a key control on interior [O_2] variability. Increases in the ventilation timescale produce more effective damping of anomalies over a broader range of forcing frequencies [*Ito and Deutsch*, 2010]. Furthermore, transient warming acts to stratify the upper ocean, limiting production of anomalies; this is evident, for instance, in diminished North Pacific Mode Water formation rates during transient warming [*Xu et al.*, 2012, 2013]. Notably, as radiative forcing is allowed to stabilize and warming fully penetrates into the subsurface, mode water formation can recover [*Xu et al.*, 2012], which might indicate that interannual variability in [O_2] is recoverable as climate stabilizes (presuming [O_2] remains greater than zero).

3.2. Changes in State

In order to estimate ToE on the basis of state anomalies, we must quantify the statistical distribution of [O_2] in an unperturbed climate state. Obtaining robust estimates of the mean and variability in [O_2] from the CESM-LE control simulation is hampered by model drift (described above), which limits our ability to use portions of this run beyond the 251 years corresponding to 1850–2100. Since it is desirable to have a larger sample size from which to estimate the [O_2] variability, we use the full ensemble during the period 1920–1950 as representative of the unperturbed climate (i.e., $\bar{c}(x)$). The 24 ensemble members over this 31 year period yields 744 simulated years, thereby providing robust statistics. We compute the mean and standard deviation of [O_2] from the 1920–1950 period and construct a signal to noise ratio as

$$S/N = -\psi_i'(x, t)/\sigma_c,$$

where σ_c is the standard deviation of annual means in the unperturbed climate. We then evaluate each transient integration to determine the point in time when the S/N exceeds 2 and remains above this threshold for the remainder of this simulation.

Natural variability in [O_2] (σ_c) on $\sigma_\theta = 26.5$ is largest near-surface outcrops, most notably in the subpolar North Pacific (Figure 6a); additionally, strong variability is found at the margins between ventilated regions and suboxic zones, such as in the southeastern Pacific, as well as the south Atlantic and Indian basins. The distribution of state-based ToE estimates suggests that detection of the forced signal should already be possible in the tropical Atlantic (Figure 6b). Similarly, early detection is possible in the south Indian Ocean, where simulated natural variability is low (Figure 6a). The North Pacific shows a relatively homogeneous distribution of ToE, with values in the range of about 2030–2040s. Notably, given the high variability in the subpolar North Pacific, ToE in this region requires [O_2] anomalies on the order of 100 mmol m^{-3}. In some regions, ToE was not possible even by 2100 (Figure 2b, gray shading). In many cases, these are regions where 21st century O_2 declines are either very small or [O_2] is actually increasing weakly (Figure 4a); much of the subtropical North Atlantic is an exception in this regard—here the variability simply continues to swamp the forced signal through 2100. Indeed, while HOTS and OSP have ToE estimated to be well before 2050, detection of a forced decline in [O_2] was not possible at BATS through 2100 on the isopycnals considered (Table 2).

3.3. Trend Magnitudes

To evaluate ToE on the basis of changes in trend magnitude in the CESM-LE, we compute retrospective linear trends in each ensemble member starting at the year 2000 and continuing through the year 2100. For each year, we compute linear trends over record lengths from 10 to 100 years. We normalize the trends
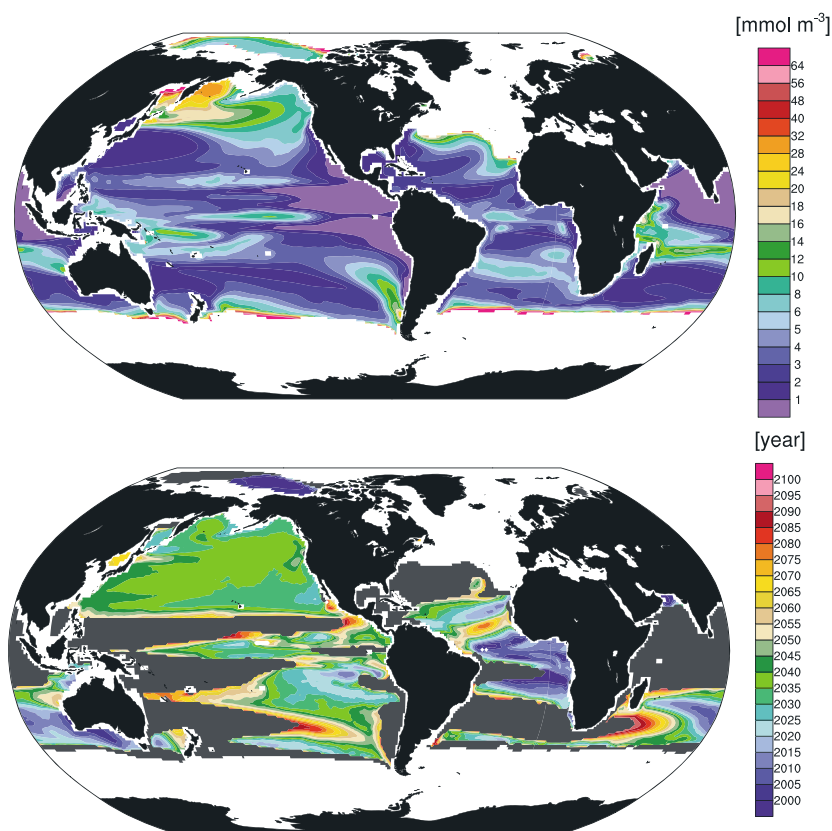
Figure 6. (a) Standard deviation of dissolved oxygen on $\sigma_\theta = 26.5$ in the CESM-LE between 1920 and 1950 (note nonlinear scale). (b) Mean time of emergence based on state anomalies on $\sigma_\theta = 26.5$ in the CESM-LE. Gray shows regions where no forced decline in oxygen was found by 2100.

computed at each year and record length by the standard deviation of trends within the full CESM-LE, yielding a signal-to-noise ratio estimate. We then diagnose ToE as the earliest year in which a trend of any length is more than 2σ outside the variability in trends across the ensemble and does not return to within 2σ for all remaining years in the simulation.

While the broad patterns of ToE based on trends (Figure 7a) are similar to those in ToE evaluated on the basis of state anomalies, there are substantial differences in detail. In particular, the trend-based methodology tends to yield earlier detection than the state anomaly approach. For instance, ToE in the subpolar northwestern Pacific is earlier on the basis of trend anomalies (2010–2020s), but detection requires relatively long (~50–60 year) records (Figure 7ab). Where ToE can be assessed in the tropical regions, detection is possible quite early, but very long records (> 60 years) are typically required. Similarly, the south Indian Ocean shows early ToE but only on the basis of long records.

Table 2. Estimated Time of Emergence (ToE) for the Anthropogenic Signal at Ocean Time Series Stations Based on the CESM-LE[a]

Station	HOT		OSP	
σ_θ	25.2	26.5	26.5	26.7
ToE (state)	2041 ± 7.1	2033 ± 5.9	2036 ± 5.0	2032 ± 5.8
ToE (trends)	2017 ± 12.1	2028 ± 5.7	2025 ± 6.8	2027 ± 8.1
Trend length	73 ± 16.6	32 ± 12.8	47 ± 15.9	50 ± 19.5

[a]ToE based on anomalies in state as well as trends are shown; see text for description of methodology. Error bounds show $\pm 1\sigma$ of ToE within the ensemble. No detectable trends were found at the Bermuda Atlantic Time Series station (BATS).
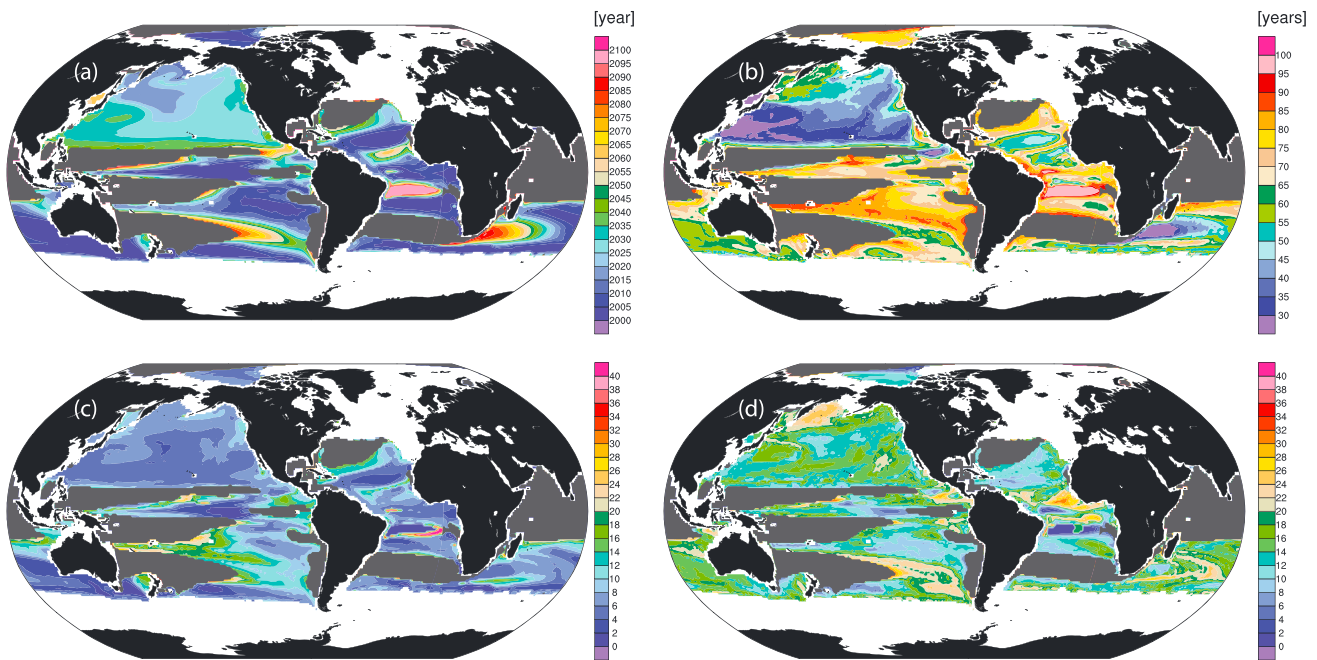
Figure 7. (a) Time of emergence (ToE) diagnosed on the basis of anomalous trend magnitudes in the CESM-LE. (b) The length of record required to ascribe ToE. (c) Standard deviation in ToE across the CESM-LE. (d) Standard deviation in the length of record. Gray shows regions where no forced decline in oxygen was found by 2100 in the ensemble mean ToE.

3.4. Spatial Structure

Our assessment of ToE on the basis of state or trend anomalies treats time series from each location as independent. It thus neglects the information contained in the spatial patterns of O_2 variability and long-term trends. If the forced signal in $[O_2]$ has a spatial structure distinct from that associated with the dominant modes of natural variability, the evolution of spatial patterns may provide detectability earlier than spatially discrete analyses. To evaluate this possibility, we compare the spatial patterns associated with forced versus natural components of variability using Empirical Orthogonal Functions (EOFs). We perform this analysis globally,
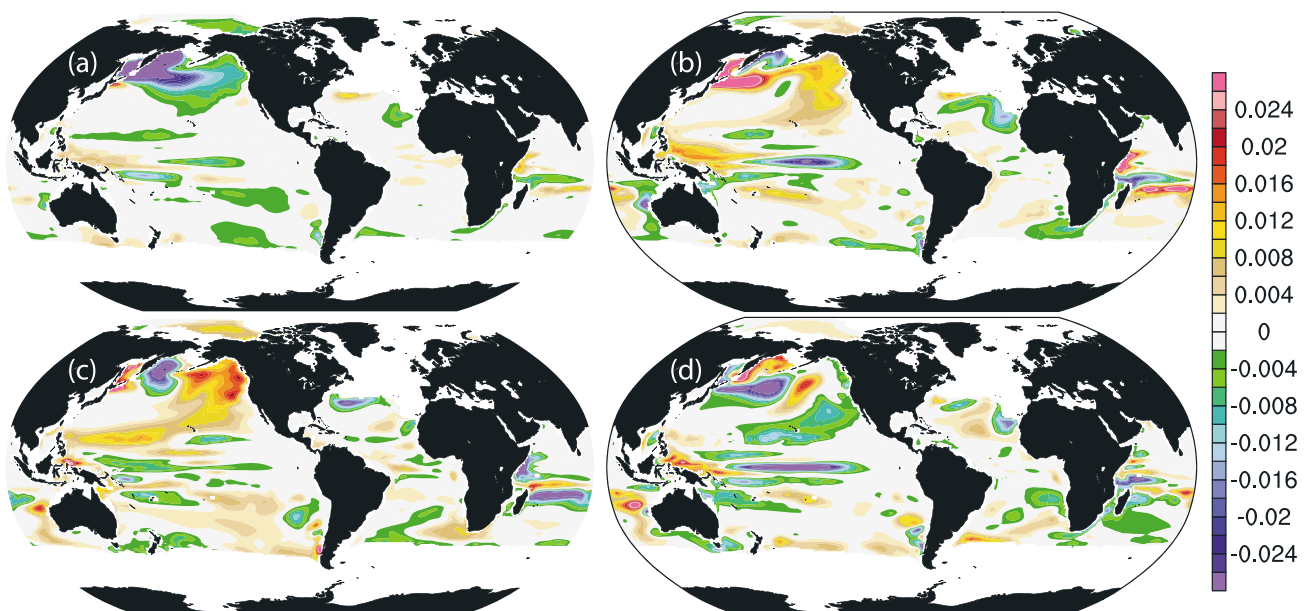

Figure 8. Spatial patterns associated with the leading EOFs of natural variability in $[O_2]$ on the $\sigma_\theta = 26.5$ isopycnal surface in CESM. (a) First EOF, variance explained = 15.6%; (b) second EOF, variance explained = 9.6%; (c) third EOF, variance explained = 6.2 %; (d) fourth EOF, variance explained = 5.1%.
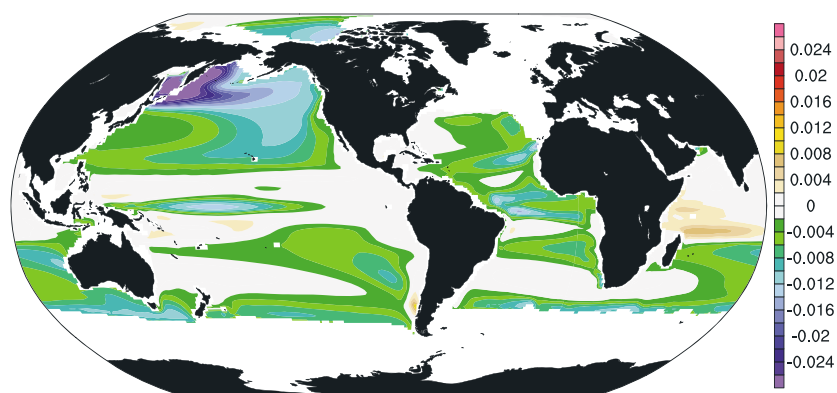
Figure 9. Spatial pattern associated with the forced signal in [O_2] on the $\sigma_\theta = 26.5$ isopycnal surface. Computed as the leading EOF from the CESM-LE ensemble mean.

noting that the overall structure of the resulting patterns is similar if the analysis is performed for each ocean basin separately.

Figure 8 shows the spatial patterns associated with the dominant modes of natural variability in [O_2] on the $\sigma_\theta = 26.5$ potential density surface computed from the CESM-LE control integration. Figure 9 shows comparable information for the forced component of variability, computed as the leading EOF in the CESM-LE ensemble mean; as expected, this plot shows a spatial structure very similar to the change in oxygen computed as a simple concentration difference (Figure 4). The leading EOF of the ensemble mean explains ∼95% of the variance in the ensemble mean data, reflecting the efficacy with which the ensemble average damps natural variability. There is also some degree of similarity between the spatial pattern associated with the forced signal (Figure 9) and the leading mode of natural variability (Figure 8) in the North Pacific where deoxygenation is particularly intense. Interannual variability modulates ventilation in this region primarily through variation in surface buoyancy forcing driving vertical exchange. Climate warming curtails ventilation as the ocean becomes increasingly stratified and its influence propagates downstream along the ventilation pathways in the subtropical thermocline over decadal timescales. While the forced signal and natural variability have similar spatial structure in the subpolar North Pacific, the forced signal is distinct over much of the subtropical thermocline. These regions are characterized by deoxygenation that is more intense on the eastern side of all basins (Figure 9).

To quantitatively assess commonality between patterns associated with forced and natural variability, we compute the fraction of spatial variance accounted for by the forced pattern over time. We project each ensemble member and the control integration onto the EOF associated with the forced signal. This projection is computed as

$$\alpha^{is}(t) = \sum_{x=1}^{p} \psi_i'(x,t)e^s(x), \tag{2}$$

for the climate anomalies from the transient integrations, and

$$\alpha^{cs}(t) = \sum_{x=1}^{p} c'(x,t)e^s(x), \tag{3}$$

for the anomalies in the control run, where $e^s(x)$ is the leading EOF of the forced signal, $\psi^s(x,t)$ (Figure 9). Following *Santer et al.* [1994], we compute the time-evolving contribution of these projections to the overall spatial variance as a means of assessing emergence of the forced pattern. The spatial variance associated with the force signal relative to the overall spatial variance is computed as

$$V_i^{is}(t) = \alpha^{is}(t)^2 \Bigg/ \sum_{x=1}^{p} \psi_i'(x,t)^2 \tag{4}$$

for each transient integration (and similarly for $c'(x,t)$).

Figure 10 shows the time evolution of the percent of spatial variance that is accounted for by the pattern associated with the forced signal. The forced signal is not wholly orthogonal to the leading modes of natural variability in the control simulation or the early portion of the transient integrations and the ensemble mean, evidenced by the nonzero contribution to the spatial variance (Figure 10). The forced signal contribution to
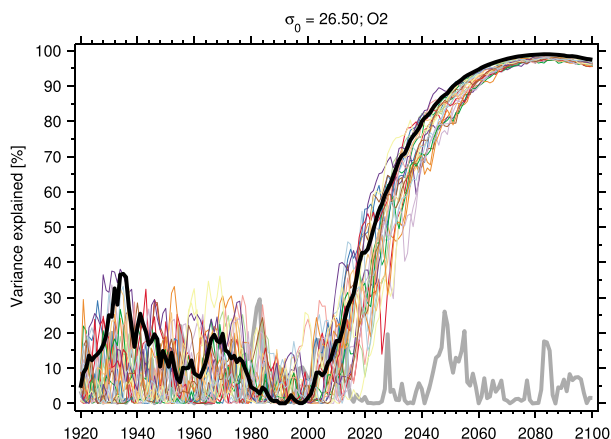
Figure 10. Temporal evolution of the percentage of total spatial variance in dissolved oxygen on the $\sigma_\theta = 26.5$ isopycnal surface attributable to the forced signal. The gray line shows the control simulation, while the black line is the ensemble mean.

spatial variance rapidly becomes dominant after about the year 2000, such that by 2020 it explains more than 40% of the spatial variance in the ensemble mean; all the ensemble members surpass this 40% threshold by about 2030. There is a minimum in the spatial variance explained by the forced signal across the ensemble just proceeding 2000. This is due to a gradual increase in the total spatial variance ($\sum_{x=1}^{P} \psi_i'(x,t)^2$) in each ensemble member through 2000. Since the spatial variance associated with the forced signal remains low and relatively constant prior to 2000, as the total spatial variance increases the percent of the spatial variance explained by the forced signal declines. The increase in the total spatial variance is likely related to the length of integration under relatively weak external forcing following initialization at 1920. Indeed, this is consistent
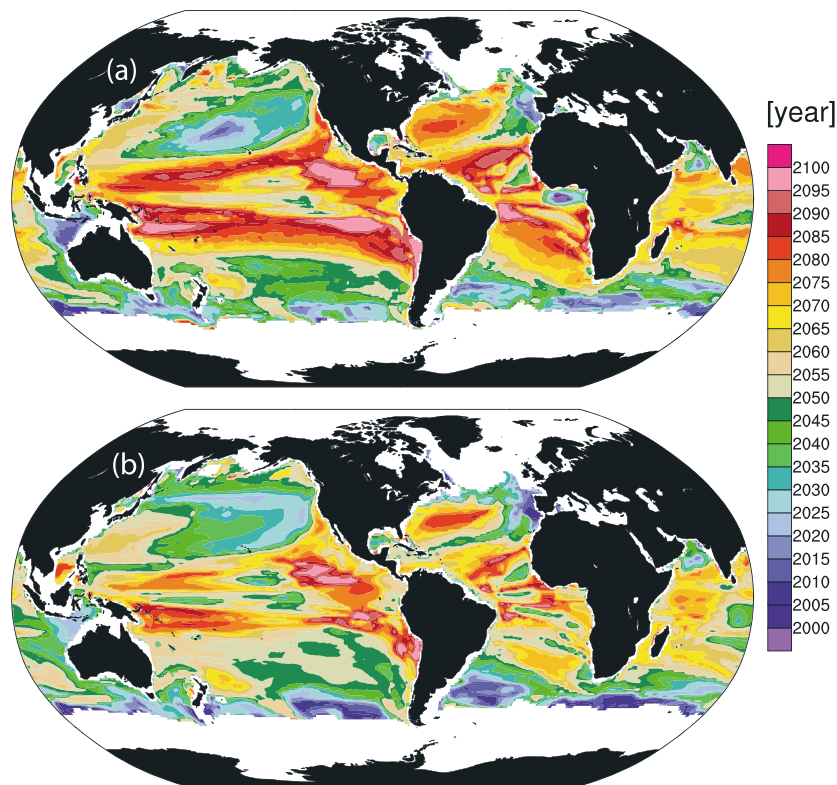

Figure 11. (a) Multimodel mean time of emergence (ToE) diagnosed on the basis of state anomalies in three CMIP5 models (GFDL, HadGEM, and MPI). (b) Multimodel mean ToE diagnosed on the basis of anomalous trends in the same three models.

with the gradual, though subtle increase in ensemble spread evident in the global O_2 inventory (Figure 1) and at time series locations (Figure 5).

3.5. Intermodel Comparison

The mean ToE from the CESM-LE falls within the range of values diagnosed from the CMIP5, both for state (Figure 11a) and trend-based anomalies (Figure 11b). The basic structure of ToE in the CMIP5 models is also similar to that in the CESM-LE, with delayed detection in the tropics, and earlier detection at midlatitude to high latitude, especially in the North Pacific. This reflects underlying similarities in the broad patterns of both the variability and late 21st century trends due to climate warming. Differences in ToE across models (not shown), however, imply that the ratio of signal to noise is not constant across models.

4. Summary and Conclusions

Dissolved oxygen in the ocean is highly sensitive to climate variability and change, in part because sea surface temperature perturbations doubly impact interior oxygen: warming reduces O_2 solubility but also stratifies the ocean limiting ventilation and O_2 supply to the interior. The first of these mechanisms is simply related to changes in ocean temperature, and can thus be evaluated from estimates of ocean heat content [*Keeling et al.*, 2010]. However, the latter reflects a more complex combination of changes in oceanic circulation and respiration rates. Historical changes in O_2 have been dominated by these latter effects (nonsolubility related), providing a critical means to assess their magnitude. However, historical O_2 changes also reveal substantial variability not characterized by a monotonic trend.

We have presented an analysis of the time required for anthropogenically forced signals in $[O_2]$ to emerge above background noise, which is the variability in $[O_2]$ driven by internal climate fluctuations. Our analysis exploits a powerful Earth system modeling approach, wherein a large ensemble of model integrations, each providing a unique realization of interannual variability, permits clear separation of externally forced and internally generated variability. We focus on $[O_2]$ on isopycnal surfaces, which highlights dynamically driven changes rather than those resulting from solubility effects.

At a global scale, anthropogenic climate change in RCP8.5 drives a sharp acceleration of oceanic deoxygenation in the first half of the 21st century (Figure 1). Deoxygenation on isopycnals within the thermocline is primarily a result of increasing stratification, which curtails supply of fresh O_2 evident in increased ventilation age. Trajectories similar to the global mean deoxygenation signal are evident at ocean time series sites (Figure 5); however, the emergence of anthropogenic signals depends on the magnitude of those signals relative to the background noise.

On the $\sigma_\theta = 26.5$ isopycnal, the subarctic North Pacific displays the most dramatic interannual variability (Figure 8). This variability delays detection of the anthropogenic signal, though since deoxygenation associated with climate warming is rather strong in this region (Figures 4a and 9), detection is possible by 2030–2040s on the basis of state anomalies and earlier on the basis of trends (Figures 6 and 7, and Table 2). Long records integrate over the periods characteristic of the dominant modes of natural variability, affording earlier ToE. The North Pacific contrasts with the southern Indian Ocean, for instance, where detection of the forced trend is possible earlier; the southern Indian Ocean has a more modest deoxygenation signal (Figure 4a) but also shows less interannual variability.

Our choice of an isopycnal framework was motivated by an interest in the dynamically-driven component of deoxygenation. An application of the ToE analysis to a depth-coordinate framework will naturally incorporate greater impacts from thermally driven solubility effects on $[O_2]$—one might expect this to afford earlier detection of the forced signal, though the depth framework is also subject to greater interannual variability associated with isopycnal heave and thus more susceptible to noise. An examination of ToE at HOT at a fixed depth of 500 m, roughly the depth of the $\sigma_\theta = 26.5$ isopycnal surface at 1920, does indicate that earlier detection is possible at this depth horizon. The mean ToE from the CESM-LE computed on the basis of trends is 2009 ± 4.5 at this location, but requires long records, in excess of 60 years; Table 2 shows the comparable mean ToE for the $\sigma_\theta = 26.5$ surface (2033 ± 5.9).

The CESM simulations tend to have oxygen concentrations that are low relative to observations, and there is some indication that the model underestimates the amplitude of interannual variability in $[O_2]$. A key question is whether low interannual variability might also be indicative of a simulated response to anthropogenic climate forcing weaker than in nature. Indeed, Table 1 suggests that the model's interannual variability is too

low and that nature has exhibited trends larger than those found in the CESM-LE. If similar physical mechanisms operate across both timescales, we might expect an association between weak interannual variability and a muted forced response. If such an association does exist, the impacts of the model biases on simulated ToE estimates may be relatively small, since the amplitude of both the signal and noise are affected, thereby preserving the ratio. The ToE estimates obtained from the CESM-LE are similar to those obtained from the CMIP5 models included in this study, suggesting that the CESM-LE can be considered representative of this broader collection of model results. In the CESM-LE, as well as in individual models of the CMIP5, there is some large-scale correspondence between interannual O_2 variance and long-term trends: regions with elevated variability also tend to show the strongest forced response. However, we found no clear intermodel relationship between the magnitude of variability and the trend driven by anthropogenic climate change. Moreover, there was no cross-model relationship between the strength of interannual variability and ToE nor between the strength of trends and ToE. We note that the biogeochemical formulations invoked by CMIP5 models, including the CESM-LE, have static structure in time, which precludes representing climate-driven changes in ecological interactions outside the domain permitted by the model parameterizations.

Observational programs might be conceived to target spatial patterns characteristic of forced declines in $[O_2]$. Unfortunately, however, the spatial pattern associated with the forced signal on the $\sigma_\theta = 26.5$ isopycnal surface (Figure 9) is not wholly distinct from the dominant modes of natural variability (Figure 8), most notably in the North Pacific. Widespread declines in $[O_2]$ in the subtropical thermocline may be an important exception; here, however, the deoxygenation signal is relatively small. An extensive network of autonomous sensors, such as profiling floats capable of measuring $[O_2]$, could possibly provide sufficient spatial coverage to capture these patterns. In the CESM-LE, there was not a significant or systematic difference between the detection time on the $\sigma_\theta = 26.5$ isopycnal surface, relative to shallower waters (e.g., Table 2). A similar insensitivity was found across the CMIP5 models, and reflects the fact that faster rates of deoxygenation are generally accompanied by higher background variability, making the signal-to-noise ratio less variable with depth than might be expected.

Our results suggest that ocean deoxygenation might already be detectable on the basis of state anomalies and/or trends in regions within the southern Indian Ocean, as well as parts of the eastern tropical Pacific and Atlantic basins. Observations have insufficient spatiotemporal coverage, however, to adequately characterize the natural $[O_2]$ distribution, in the case of evaluating state anomalies. Furthermore, in most regions where early detection is possibly, relatively long records (>50 years) are required to assess the exceedance of a trend from the O_2 variability generated in a stationary climate without external forcing. Some regions never show definitive declines in $[O_2]$ associated with the forced signal. For instance, our calculation shows that externally forced oxygen decline at BATS is weak, and detection is not expected through the end of the 21st century (Figures 6a and 7a). Thus, even perfectly precise, sustained measurements of oxygen and age tracers, would not likely permit detection of the externally forced trend in this region because the signal is too small to overcome internal variability.

In conclusion, the primary advantage of the CESM-LE is its dramatic illustration of the forced signal superimposed on natural variability. The biases in the simulation of interior O_2 make the estimates of ToE provided by the model difficult to trust precisely; however, the basic structures are likely to be robust. This framework provides a valuable context for understanding variability in historical data and observing future trajectories of change. Ultimately, comprehensive and sustained observations are needed to fully characterize internal variability and discern forced trends.

References

Andreev, A. G., and V. I. Baturina (2006), Impacts of tides and atmospheric forcing variability on dissolved oxygen in the subarctic North Pacific, *J. Geophys. Res.*, *111*, C07S10, doi:10.1029/2005JC003103.

Armstrong, R., C. Lee, J. Hedges, S. Honjo, and S. Wakeham (2002), A new, mechanistic model for organic carbon fluxes in the ocean based on the quantitative association of POC with ballast minerals, *Deep Sea Res.*, *49*(1–3), 219–236, doi:10.1016/S0967-0645(01)00101-1.

Bograd, S. J., C. G. Castro, E. Di Lorenzo, D. M. Palacios, H. Bailey, W. Gilly, and F. P. Chavez (2008), Oxygen declines and the shoaling of the hypoxic boundary in the California Current, *Geophy. Res. Lett.*, *35*, L12607, doi:10.1029/2008GL034185.

Bopp, L., C. Le Quéré, M. Heimann, A. C. Manning, and P. Monfray (2002), Climate-induced oceanic oxygen fluxes: Implications for the contemporary carbon budget, *Global Biogeochem. Cycles*, *16*(2), 1022, doi:10.1029/2001GB001445.

Brandt, P., V. Hormann, B. Bourlès, J. Fischer, F. A. Schott, L. Stramma, and M. Dengler (2008), Oxygen tongues and zonal currents in the equatorial Atlantic, *J. Geophys. Res.*, *113*, C04012, doi:10.1029/2007JC004435.

Brandt, P., R. J. Greatbatch, M. Claus, S.-H. Didwischus, V. Hormann, A. Funk, J. Hahn, G. Krahmann, J. Fischer, and A. Körtzinger (2012), Ventilation of the equatorial Atlantic by the equatorial deep jets, *J. Geophys. Res.*, *117*, C12015, doi:10.1029/2012JC008118.

Branstator, G., and H. Teng (2010), Two limits of initial-value decadal predictability in a CGCM, *J. Clim.*, *23*, 6292–6311, doi:10.1175/2010JCLI3678.1.

Christian, J. R. (2014), Timing of the departure of ocean biogeochemical cycles from the preindustrial state, *PLoS One*, *9*(11), e109820, doi:10.1371/journal.pone.0109820.

Cocco, V., et al. (2013), Oxygen and indicators of stress for marine life in multi-model global warming projections, *Biogeosciences*, *10*, 1849–1868, doi:10.5194/bg-10-1849-2013.

Collins, W. J., et al. (2011), Development and evaluation of an Earth-system model – HadGEM2, *Geosci. Model Dev.*, *4*(4), 1051–1075, doi:10.5194/gmd-4-1051-2011.

Danabasoglu, G., S. C. Bates, B. P. Briegleb, S. R. Jayne, M. Jochum, W. G. Large, S. Peacock, and S. G. Yeager (2012), The CCSM4 ocean component, *J. Clim.*, *25*(5), 1361–1389, doi:10.1175/JCLI-D-11-00091.1.

Deser, C., A. Phillips, V. Bourdette, and H. Teng (2012), Uncertainty in climate change projections: the role of internal variability, *Clim. Dyn.*, *38*, 527–546, doi:10.1007/s00382-010-0977-x.

Deutsch, C., S. Emerson, and L. Thompson (2006), Physical-biological interactions in North Pacific oxygen variability, *J. Geophys. Res.*, *111*, C09S90, doi:10.1029/2005JC003179.

Deutsch, C., H. Brix, T. Ito, H. Frenzel, and L. Thompson (2011), Climate-forced variability of ocean hypoxia, *Science*, *333*, 336–339, doi:10.1126/science.1202422.

Devries, T., and C. Deutsch (2014), Large-scale variations in the stoichiometry of marine organic matter respiration, *Nat. Geosci.*, *7*, 890–894, doi:10.1038/ngeo2300.

Dietze, H., and U. Loeptien (2013), Revisiting "nutrient trapping" in global coupled biogeochemical ocean circulation models, *Global Biogeochem. Cycles*, *27*, 265–284, doi:10.1002/gbc.20029.

Doney, S. C., L. Bopp, and M. C. Long (2014), Historical and future trends in ocean climate and biogeochemistry, *Oceanography*, *27*(1), 109–119, doi:10.5670/oceanog.2014.14.

Dunne, J. P., et al. (2012), GFDL's ESM2 global coupled climate-carbon earth system models. Part I: Physical formulation and baseline simulation characteristics, *J. Clim.*, *25*, 6646–6665, doi:10.1175/JCLI-D-11-00560.1.

Dunne, J. P., et al. (2013), GFDL's ESM2 global coupled climate-carbon Earth system models. Part II: Carbon system formulation and baseline simulation characteristics, *J. Clim.*, *26*, 2247–2267, doi:10.1175/JCLI-D-12-00150.1.

Duteil, O., F. U. Schwarzkopf, C. W. Böning, and A. Oschlies (2014), Major role of the equatorial current system in setting oxygen levels in the eastern tropical Atlantic Ocean: A high-resolution model study, *Geophy. Res. Lett.*, *41*, 2033–2040, doi:10.1002/2013GL058888.

Emerson, S., Y. Watanabe, T. Ono, and S. Mecking (2004), Temporal trends in apparent oxygen utilization in the upper pycnocline of the North Pacific: 1980–2000, *J. Oceanogr.*, *60*(1), 139–147, doi:10.1023/B:JOCE.0000038323.62130.a0.

Garcia, H. E., T. P. Boyer, S. Levitus, R. A. Locarnini, and J. Antonov (2005), On the variability of dissolved oxygen and apparent oxygen utilization content for the upper world ocean: 1955 to 1998, *Geophy. Res. Lett.*, *32*, L09604, doi:10.1029/2004GL022286.

Garcia, H. E., R. A. Locarnini, T. P. Boyer, J. I. Antonov, A. V. Mishonov, O. K. Baranova, M. M. Zweng, J. R. Reagan, and D. R. Johnson (2014), World Ocean Atlas 2013, in *Volume 3: Dissolved Oxygen, Apparent Oxygen Utilization, and Oxygen Saturation*, edited by S. Levitus and A. Mishonov, 27 pp., NOAA Atlas NESDIS 75, Silver Spring, Md.

Getzlaff, J., and H. Dietze (2013), Effects of increased isopycnal diffusivity mimicking the unresolved equatorial intermediate current system in an earth system climate model, *Geophy. Res. Lett.*, *40*, 2166–2170, doi:10.1002/grl.50419.

Giorgetta, M. A., et al. (2013), Climate and carbon cycle changes from 1850 to 2100 in MPI-ESM simulations for the Coupled Model Intercomparison Project phase 5, *J. Adv. Model. Earth Syst.*, *5*, 572–597, doi:10.1002/jame.20038.

HadGEM2 Development Team (2011), The HadGEM2 family of Met Office Unified Model climate configurations, *Geosci. Model Dev.*, *4*(3), 723–757, doi:10.5194/gmd-4-723-2011.

Hasselmann, K. (1976), Stochastic climate models part I. Theory, *Tellus*, *28*(6), 473–485, doi:10.1111/j.2153-3490.1976.tb00696.x.

Hasselmann, K. (1993), Optimal fingerprints for the detection of time-dependent climate change, *J. Clim.*, *6*(10), 1957–1971, doi:10.1175/1520-0442(1993)006<1957:OFFTDO>2.0.CO;2.

Helm, K. P., N. L. Bindoff, and J. A. Church (2011), Observed decreases in oxygen content of the global ocean, *Geophy. Res. Lett.*, *38*, L23602, doi:10.1029/2011GL049513.

Holland, M. M., D. A. Bailey, B. P. Briegleb, B. Light, and E. Hunke (2012), Improved sea ice shortwave radiation physics in CCSM4: The impact of melt ponds and aerosols on Arctic Sea Ice, *J. Clim.*, *25*(5), 1413–1430, doi:10.1175/JCLI-D-11-00078.1.

Hunke, E., and W. Lipscomb (2008), CICE: The Los Alamos sea ice model, documentation and software user's manual, version 4.0, *Tech. Rep. LA-CC-06-012*, Los Alamos Natl. Lab., Los Alamos, N. M.

Hurrell, J. W., et al. (2013), The community earth system model: A framework for collaborative research, *Bull. Am. Meteorol. Soc.*, *94*, 1339–1360, doi:10.1175/BAMS-D-12-00121.1.

Ito, T., and C. Deutsch (2010), A conceptual model for the temporal spectrum of oceanic oxygen variability, *Geophy. Res. Lett.*, *37*, L03601, doi:10.1029/2009GL041595.

Johnson, G. C., and N. Gruber (2007), Decadal water mass variations along 20°W in the Northeastern Atlantic Ocean, *Prog. Oceanogr.*, *73*, 277–295, doi:10.1016/j.pocean.2006.03.022.

Kay, J. E., et al. (2014), The Community Earth System Model (CESM) large ensemble project: A community resource for studying climate change in the presence of internal climate variability, *Bull. Am. Meteorol. Soc.*, *96*, 1333–1349, doi:10.1175/BAMS-D-13-00255.1.

Keeling, R. F., and H. E. Garcia (2002), The change in oceanic O_2 inventory associated with recent global warming, *Proc. Natl. Acad. Sci. U.S.A.*, *99*(12), 7848–7853, doi:10.1073/pnas.122154899.

Keeling, R. F., A. Körtzinger, and N. Gruber (2010), Ocean deoxygenation in a warming world, *Annu. Rev. Mar. Sci.*, *2*, 199–229, doi:10.1146/annurev.marine.010908.163855.

Long, M. C., K. Lindsay, S. Peacock, J. K. Moore, and S. C. Doney (2013), Twentieth-century oceanic carbon uptake and storage in CESM1(BGC), *J. Clim.*, *26*(18), 6775–6800, doi:10.1175/JCLI-D-12-00184.1.

Long, M. C., K. Lindsay, and M. M. Holland (2015), Modeling photosynthesis in sea ice covered waters, *J. Adv. Model. Earth Syst.*, *7*, 1189–1206, doi:10.1002/2015MS000436.

Meinshausen, M., et al. (2011), The RCP greenhouse gas concentrations and their extensions from 1765 to 2300, *Clim. Change*, *109*, 213–241, doi:10.1007/s10584-011-0156-z.

Moore, J. K., K. Lindsay, S. C. Doney, M. C. Long, and K. Misumi (2013), Marine ecosystem dynamics and biogeochemical cycling in the Community Earth System Model [CESM1(BGC)]: Comparison of the 1990s with the 2090s under the RCP4.5 and RCP8.5 scenarios, *J. Clim.*, *26*(23), 9291–9312, doi:10.1175/JCLI-D-12-00566.1.

Nakamura, T., T. Toyoda, Y. Ishikawa, and T. Awaji (2006), Effects of tidal mixing at the Kuril Straits on North Pacific ventilation: Adjustment of the intermediate layer revealed from numerical experiments, *J. Geophys. Res.*, *111*, C04003, doi:10.1029/2005JC003142.

Ono, T., T. Midorikawa, Y. W. Watanabe, K. Tadokoro, and T. Saino (2001), Temporal increases of phosphate and apparent oxygen utilization in the subsurface waters of western subarctic Pacific from 1968 to 1998, *Geophy. Res. Lett.*, *28*(17), 3285–3288, doi:10.1029/2001GL012948.

Plattner, G.-K., F. Joos, and T. F. Stocker (2002), Revision of the global carbon budget due to changing air-sea oxygen fluxes, *Global Biogeochem. Cycles*, *16*(4), 1096, doi:10.1029/2001GB001746.

Santer, B. D., W. Brüggemann, U. Cubasch, K. Hasselmann, H. Höck, E. Maier-Reimer, and U. Mikolajewica (1994), Signal-to-noise analysis of time-dependent greenhouse warming experiments, *Clim. Dyn.*, *9*, 267–285, doi:10.1007/BF00204743.

Santer, B. D., et al. (2011), Separating signal and noise in atmospheric temperature changes: The importance of timescale, *J. Geophys. Res.*, *116*, D22105, doi:10.1029/2011JD016263.

Sasano, D., Y. Takatani, N. Kosugi, T. Nakano, T. Midorikawa, and M. Ishii (2015), Multidecadal trends of oxygen and their controlling factors in the western North Pacific, *Global Biogeochem. Cycles*, *29*, 935–956, doi:10.1002/2014GB005065.

Smith, R. D., et al. (2010), The Parallel Ocean Program (POP) reference manual, *Tech. Rep. LAUR-10-01853*, Los Alamos Natl. Lab., Los Alamos, N. M. [Available at http://www.cesm.ucar.edu/models/cesm1.0/pop2/doc/sci/POPRefManual.pdf.]

Stanley, R. H. R., S. C. Doney, W. J. Jenkins, and D. E. Lott III (2012), Apparent oxygen utilization rates calculated from tritium and helium-3 profiles at the Bermuda Atlantic Time-series Study site, *Biogeosciences*, *9*, 1969–1983, doi:10.5194/bg-9-1969-2012.

Stendardo, I., and N. Gruber (2012), Oxygen trends over five decades in the North Atlantic, *J. Geophys. Res.*, *117*, C11004, doi:10.1029/2012JC007909.

Stramma, L., G. C. Johnson, J. Sprintall, and V. Mohrholz (2008), Expanding oxygen-minimum zones in the tropical oceans, *Science*, *320*, 655–658, doi:10.1126/science.1153847.

Taylor, K. E., R. J. Stouffer, and G. A. Meehl (2012), An overview of CMIP5 and the experiment design, *Bull. Am. Meteorol. Soc.*, *93*, 485–498, doi:10.1175/BAMS-D-11-00094.1.

van Aken, H. M., M. Femke de Jong, and I. Yashayaev (2011), Decadal and multi-decadal variability of Labrador Sea Water in the north-western North Atlantic Ocean derived from tracer distributions: Heat budget, ventilation, and advection, *Deep Sea Res.*, *58*, 505–523, doi:10.1016/j.dsr.2011.02.008.

Whitney, F. A., H. J. Freeland, and M. Robert (2007), Persistently declining oxygen levels in the interior waters of the eastern Subarctic Pacific, *Prog. Oceanogr.*, *75*, 179–199, doi:10.1016/j.pocean.2007.08.007.

Xu, L., S.-P. Xie, and Q. Liu (2012), Mode water ventilation and subtropical countercurrent over the North Pacific in CMIP5 simulations and future projections, *J. Geophys. Res.*, *117*, C12009, doi:10.1029/2012JC008377.

Xu, L., S.-P. Xie, and Q. Liu (2013), Fast and slow responses of the North Pacific mode water and subtropical countercurrent to global warming, *J. Ocean Univ. Chin.*, *12*, 216–221, doi:10.1007/s11802-013-2189-6.